

## Experimental investigation of an Organic Rankine Cycle Tesla turbine working with R1233zd(E)



Lorenzo Talluri<sup>a</sup>, Olivier Dumont<sup>b</sup>, Giampaolo Manfrida<sup>a</sup>, Vincent Lemort<sup>b</sup>, Daniele Fiaschi<sup>a,\*</sup>

<sup>a</sup> Dipartimento di Ingegneria Industriale, Università degli Studi di Firenze Viale Morgagni 40, 50135 Firenze, Italy

<sup>b</sup> Thermodynamics Laboratory, University of Liège, 4000 Liège, Belgium

### HIGHLIGHTS

- Performance measurement of an Organic Rankine Cycle Tesla turbine prototype.
- Experimental evaluation and modelling of disks edge and ventilation losses.
- Validation and improvement of 2D calculation model against experimental results.
- Thermodynamically, the non-optimized prototype achieved 906 W at 30% efficiency.
- Maximum achieved shaft efficiency was of 9.62% and maximum achieved shaft power was of 371 W.

### ARTICLE INFO

**Keywords:**  
Tesla turbine  
Fluid dynamics  
ORC  
Micro expanders  
Experimental campaign

### ABSTRACT

The increasing interest in micro power generation is pushing the research world to find new solutions for increasing the efficiency of micro Organic Rankine Cycles. One of their main issues is the efficiency and the reliability of the expander. The Tesla turbine is an old/new expander, which has found a renewed interest in the last years because of the increasing appeal towards distributed micro generation, where this expander becomes competitive.

This peculiar technology seems adapted to micro generation in Organic Rankine Cycle thanks to its main characteristic, which is its simple structure that allows for high reliability and cheapness. In recent years, this expander has been analytically and numerically assessed when working with organic fluids. In this study, the experimental investigation of a Tesla turbine working with R1233zd(E) is presented. One of the main achievements was the assessment of the blockage effect of disks edges when the pressure drop through the machine is relevant as in case of Organic Rankine Cycles (e.g. higher than 3–4 bars), resulting into a relatively large amount of flow deviation through the clearances between the rotor disks package and the case, which implies a throttling effect thus resulting into a relevant performance loss. This effect was accounted by a model that well fitted the experimental data.

The achieved results confirmed the validity and the large applications potential of this emerging technology, especially in the fields of micro power generation, low inlet temperature and low expansion ratios. A maximum net power output of 371 W was obtained, proving the feasibility of utilizing Tesla turbines in Organic Rankine Cycle applications. A maximum shaft efficiency of 9.62% and a maximum adiabatic efficiency of 30% were achieved. The results and the developed model of disks edge losses effects represent an important step ahead, in physical depiction of the phenomenology, over the currently available literature, fundamental for the improvement of the design procedure of Tesla turbines for Organic Rankine Cycles.

### 1. Introduction

In recent years, the sustainability of the energy sector has become the focus of the research word, as global warming is turning into a very pressing issue. The improvement of energy efficient utilization has

therefore grow into one of the most assessed subject in order to mitigate the climate change. Nowadays, there is still a very big portion of low temperature heat which is wasted to the atmosphere, that could be instead recovered. Most of the wasted heat comes from industrial processes, or from the exhaust gases of internal combustion engines (ICE),

\* Corresponding author.

E-mail address: [daniele.fiaschi@unifi.it](mailto:daniele.fiaschi@unifi.it) (D. Fiaschi).

<b>Nomenclature</b>	
$\dot{m}$	Mass flow rate [kg/s]
A	Area [ $m^2$ ]
a	Axial velocity profile control coefficient
b	Channel height [m]
C	Coefficient
d	Diameter
F	Friction factor [-]
H	Height [m]
$H_s$	Stator height [m]
M	Moment [Nm]
P	Power [W]
P	Pressure [Pa]
r	Radius [m]
s	Disks thickness [m]
T	Temperature [ $^{\circ}$ C]
TW	Throat width [m]
<i>Greek symbols</i>	
$\eta$	Efficiency [-]
$\varepsilon$	Partialization degree [-]
$\rho$	Density [ $kg/m^3$ ]
$\omega/\Omega$	Rotational speed [rad/s]
$\nu$	kinematic viscosity [ $m^2/s$ ]
<i>Subscripts and superscripts</i>	
0.3	Turbine ref. sections
ad	Adiabatic
t	Tangential

which have the very suited characteristics to feed organic Rankine cycles (ORC). The ORC systems are becoming indeed the leading technology for low temperature - low power applications. Many researchers have performed comprehensive investigations on several aspects of ORCs, including thermodynamic design and optimization [1,2], working fluid selection [3,4], architecture assessment [5,6], expanders [7,8] and applications [9,10].

Out of so many different researches, it is emerged that the efficiency of the expander within an ORC power plant is one of the key variables, which deeply influences the performance of the cycle [7,11]. Due to the many and varied applications [11–13], as well as to the several possible working fluids [14] and the power ranges, it is not possible to identify an optimal expander for an ORC. Nonetheless, best practices have been draught for each application, showing the advantages and disadvantages of each expander technology. Generally, axial turbines are predominant for large power applications ( $> 500$  kWe), radial turbines are the main technology for medium range applications (50–500 kW), while for mini and small-scale systems several expander technologies (mainly volumetric) are present [7,15–18].

Generally, dynamic expanders (axial and radial turbines) are not suited for mini and micro-power applications due to the requirements of very high rotational speed for the lower power ranges [19,20]. However, there have been some studies on the application of axial and radial turbines for small scale ORCs [21,22]. The most suited technology for micro/minи scale applications depends on several parameters, such as cycle architecture, operating conditions, boundary conditions, cost constraints, working fluid, compactness, size; nevertheless the most common used mini/micro expanders are volumetric expanders, such as the roots, the scroll, the screw and the piston expanders.

Particularly, piston expanders are best fitted for small volume flow rates ( $< 75$  l/s) and low power applications ( $\sim 10$  kW). The average efficiency is a little below 70% and they are able to work at high inlet temperatures, high inlet pressures and large pressure ratios [23]. The possibility of working with very high pressure ratio ( $> 14$ ), is the main feature of this technology, which allows it to be utilized in several applications.

Another very utilized expander is the scroll, which is characterised by very few rotating parts, which allows it to be a reliable and efficient expander. Nevertheless, conversely to piston expanders, the scroll expander does not allow high pressure ratio; it presents, indeed, a limited expansion pressure ratio, due to the maximum volume ratio, which is commonly limited to 4.2 [23]. In order to contrast this issue, a proposed solution is to achieve a higher pressure ratio through the connection of two expanders in series [24]. One other very interesting feature is the

ability to handle very high mass fractions of liquid ( $> 80\%$ ) as experimentally validated in [25], where a liquid flooded scroll was tested with an aqueous ethylene glycol mixture.

Compared to scroll and piston expanders, the screw expanders have several advantages, such as the possibility of achieving very high shaft speeds (20,000 RPM), the compactness and capability of handling wet expansions ( $> 90\%$ ). Nonetheless, due to the higher production costs, they are commonly used for applications in a power range slightly higher than scroll or piston expanders, even if they could achieve high efficiency even at micro power level applications.

Finally, roots expanders are not commonly used. Indeed, even the scientific literature about these machines is limited. Their main characteristic is to show a volume ratio usually close to one, limiting therefore their expansion ratio. Their main field of application is therefore the low pressure, low expansion ratio, with a power range approximately from 1 to 30 kW, with maximum rotational speed of about 20,000 rpm. Similarly, to scroll and screw, also this type of expander can handle a quite large fraction of liquid during the expansion process [23].

Table 1 reports some of the experimental investigation on mini and micro expanders which have been performed in the last years.

Fig. 1 displays the four different expander technologies with the addition of a new expander, which in the last years is stirring up interest in the research community and specifically in the field of micro

**Table 1**  
Experimental investigations on mini and micro expander.

Reference	Expander Technology	Working Fluid	Power output [kW]	Efficiency [%]	Rotational speed [rpm]
[21]	Axial Impulse Turbine	Cyclopentane MM	15 12	65 73.4	30,000 24,000
[22]	Radial Turbine	R245fa	32.70	78.7	20,000
[26]	Scroll	HCFC-123	1.80	68	1770
[27]	Scroll	R123	1.54	86	2165
[28]	Scroll	R245fa	1.80	75.7	3500
[29]	Screw	R123	8.35	73	3000
[30]	Screw	R245fa SES36	6.87 7.36	64.7 51.9	3000 3000
[31]	Piston	R134a	1.15	42	800
[32]	Piston	R245fa	0.35	40	645
[23]	Piston	R245fa	2.7	53	2000
	Screw		1.29	53	6000
	Scroll		1.54	76	3000
	Roots		3.05	47	5000

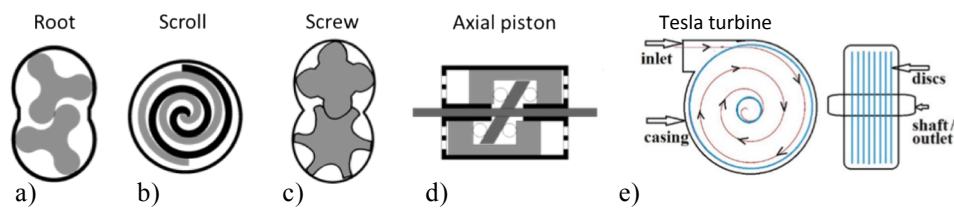


Fig. 1. Different expander technologies [24,33].

power generation: the Tesla turbine.

Fig. 2 highlights the main characteristics of volumetric expander, axial and radial turbines and Tesla turbines. Of particular interest is that Tesla turbine characteristics are closer to those of volumetric expander such as rotational speed, power, pressure and temperature operational ranges; with the only exception of the quasi-independency of pressure ratio with rotational speed, proper of dynamic machines.

## 2. Tesla turbine

Conversely to traditional turbomachines, which exploit the pressure difference that is produced when a fluid flows around a row of blades; the Tesla turbine generates power through the frictional interaction between the evolving fluid and the bladeless rotor. This peculiar rotor, characterized by the absence of blades, is the main feature of the Tesla turbine. Indeed, differently from conventional turbines, the rotor is composed by a series of parallel flat disks with a very small gap between them. The admission of the flow in the rotor occurs through one or more nozzles, which allows the fluid to enter from the external radius of the disks and to exit from the openings made on the disks at the inner radius. Inside the rotor, the fluid depicts a spiral centrifugal path, due to the interaction between the viscous forces and exchange of momentum.

Typical configurations of the Tesla turbine consider only the rotor as part of the turbine, and often, nozzles are just converging pipes positioned tangentially to the rotor outer radius, as displayed in Fig. 3.

The first concept of the Tesla turbine was conceived by the Serbian

Engineer N. Tesla in 1913 [38]. In his work, which resulted in a patent, he clearly explained the principle of operation of the machine, as well the first schematic of prototype. Nonetheless, due to the coming of gas turbines and to the run towards large size power plants, coupled to the poor experimental performance of this expander, especially for high power applications, this technology found neither any commercial nor research engagement until 1950. At that time a couple of research assessment were carried out. Leaman [39] built and tested a 130 mm rotor diameter turbine utilizing air as working fluid, achieving 87 W power output and an efficiency of 8.6%. Armstrong [34] designer, realized and tested an air Tesla turbine, focusing its work on the analysis of inefficiencies. The main obtained result was the identification of the nozzle losses as the main contributor to the low efficiency of the expander.

In the following years (1960 s) some further research was carried out mainly by W. Rice, who developed a comprehensive know-how on the Tesla turbine. Among his research, he developed an analytical solution of the flow running inside the plates of a Tesla turbine and performed a quite extensive experimental test campaign on several prototypes with air as working fluid [35]. Particularly, he designed and tested 6 different configurations of the turbine, discovering that best efficiencies were achieved when low mass flow rates were tested. After W. Rice works (which accounted for a scientific production of > 10 papers), the Tesla turbine "went back in the darkness", until recent years, as only spot researches, such as that of Allen in 1990 [40] were produced.

It is only in recent years, due to the renewed and growing interests

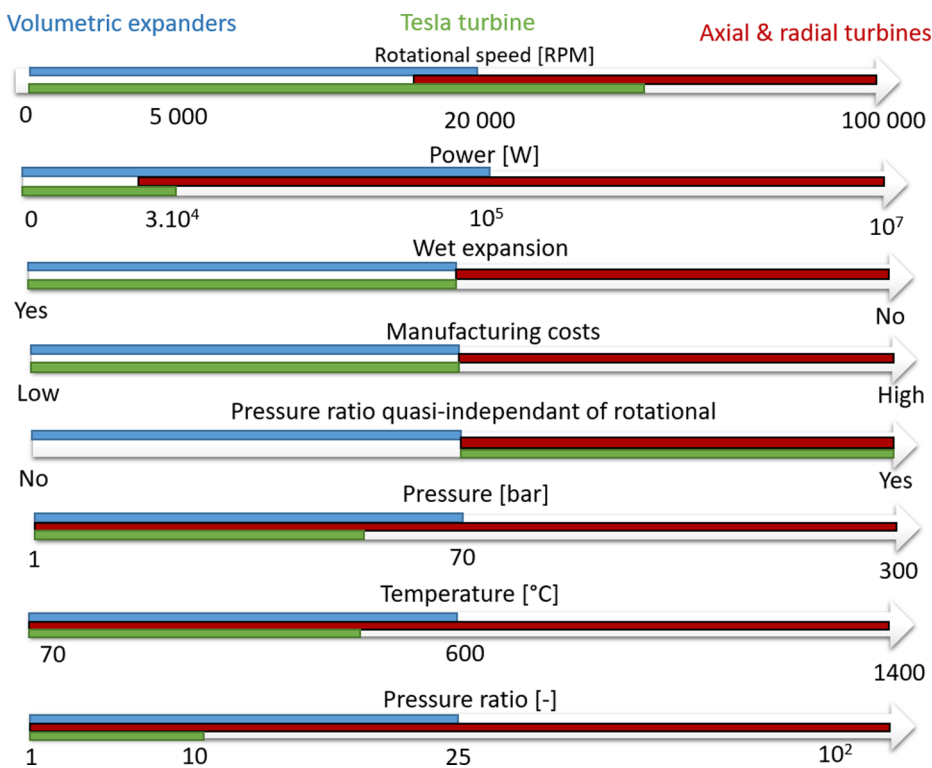


Fig. 2. Comparison of volumetric expanders, axial/radial turbines and Tesla turbines.

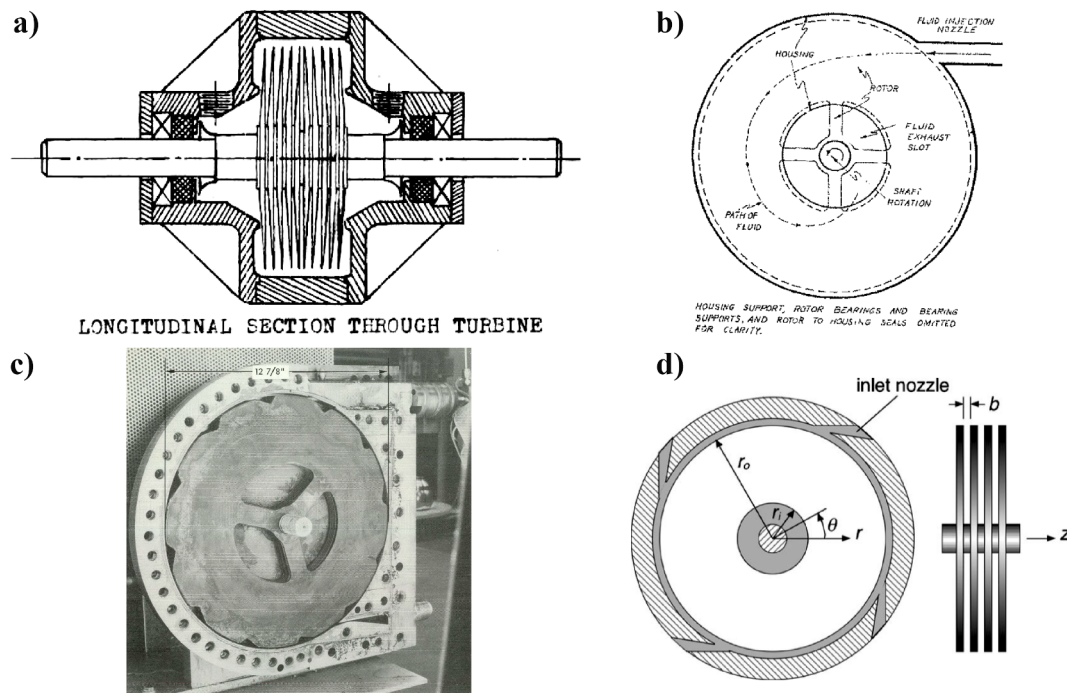


Fig. 3. Typical configuration of Tesla turbine a) [34], b) [35], c) [36], d) [37].

towards distributed power generation, that the research on the Tesla turbine has flourished.

Several authors started developing research on the air Tesla turbine, from analytical works to computational and experimental.

A significant contribution to the literature of Tesla turbines has been given by the research carried out by Guha and Sengupta. Indeed, these researchers developed a comprehensive analytical model, which was validated and compared with computational fluid dynamics calculations [41], that has been the basis for the development and understanding of the fluid flow features inside a Tesla turbine rotor. Particularly, the influence of each acting force on the flow of a Tesla turbine rotor were assessed and depicted, allowing the understanding of the behaviour, as well as the cause of inefficiency [42]. Another important line of research on Tesla turbines was carried out by Carey, who also developed an analytical model for the performance assessment of the expander [37]. Conversely to the model developed by Guha and Sengupta (which reduced the Navier Stokes equation assuming a viscous flow), Carey assumed an inviscid fluid, considering the impact of viscous effect as body forces. This allowed a simplification of the model that was also applied to design, build and test a mm-scale turbine [43].

Another relevant line of research is the one lead by Schosser and Pfitzner [44,45], which designed and built a test rig for the measuring of the velocity of the flow of an air driven Tesla turbine. Particularly, PIV measurement was utilized in order to draw the velocity profile, which was found to be slightly different than the commonly assumed parabolic profile; it was found that a 4th order polynomial better approximate the velocity distribution.

Other studies on Tesla turbines have dealt performance assessment through the means of CFD [46,47] and experimental campaigns [48–51].

Finally, in recent years, the application of the Tesla turbine as an expander for ORC was assessed by an increasing number of researchers. Lampart and Jedrzejewski [52] developed an extensive CFD assessment on a 32 cm rotor diameter, achieving 51% efficiency with a mass flow rate of 0.13 kg/s of Solkatherm SES36. Song *et al.* [53] developed an analytical model of Tesla turbines for ORC applications and compared it with the results obtained by Rice [54]. The model was coupled with an ORC in order to assess the cycle performance. At design point, the ORC

with R245ca released 1.25 kW power output with 4% thermodynamic cycle efficiency.

The authors also contributed to the literature on Tesla turbine for ORC through the development of several studies. The main ones deal with the revision of the configuration of the turbine [55,56], the development of a new analytical model [57,58], the numerical investigation of the rotor with several working fluids [59,60] and the comparison with other micro expanders for micro and mini ORC [61].

The literature review shows that several analytical and numerical models have been developed, and many experimental studies on air Tesla turbine have been carried out; but experimental results of a Tesla turbine working with an organic fluid (and in particular with R1233zd (E)) seems to be still missing in literature. Therefore, the main goal of this study is to present the obtained experimental results and to expose the pros and cons of the machine, demonstrating the possibility of using a Tesla turbine for micro ORC applications.

## 2.1. Prototype geometry

Conversely to the typical configurations, the Tesla turbine prototype utilised in the present test campaigns is made by several components: an external toroidal plenum chamber, a stator with fixed nozzles and a bladeless rotor, composed by parallel thin disks fixed to the rotating shaft. The sizing of each part of the machine was carried out taking into account both fluid dynamics and mechanical aspects, as reported in [55,56]. The resulting dimensions of the prototype are reported in Table 2.

The stator is divided into 30 “disk layers”, each one containing four nozzles of 1 mm height ( $H_s$ ) and 1 mm of throat width (TW), which allow tangential admission to the rotor (exit nozzle angle is of 85°). Each stator provides the mass flow rate to 2 rotor channels; the rotor is made of 60 channels in total. Two different disks thickness ( $s$ ) were considered: 0.8 and 1 mm, in order to properly match the stator channels heights and thus having 0.1 mm width rotor channels (b). Fig. 4 displays the schematic of the ORC prototype.

**Table 2**  
Turbine geometry.

Component	Parameter	Value	Unit
Stator	Outer casing radial minimum thickness	0.02	[m]
	Outer casing internal radius	0.33	[m]
	Height of plenum chamber	0.03	[m]
	Stator inlet radius ( $r_0$ )	0.136	[m]
	Stator outlet radius ( $r_1$ )	0.1085	[m]
	Nozzle throat height ( $H_s$ )	0.001	[m]
	Nozzle throat width ( $TW$ )	0.001	[m]
	Chord length	0.059	[m]
	Stator inlet angle (radial direction)	0	[°]
	Stator outlet angle (radial direction)	85	[°]
Stator/Rotor Rotor	Number of nozzles for each vane	4	[‐]
	Gap	0.001	[m]
	Rotor inlet radius ( $r_2$ )	0.108	[m]
	Rotor outlet radius ( $r_3$ )	0.0275	[m]
	Channel height ( $b$ )	0.0001	[m]
Disk thickness ( $s$ )	0.001/	[m]	
	0.0008	[m]	
Number of rotor channels		60	[‐]

## 2.2. Test bench description

The schematic of the test bench available at the Thermodynamic laboratory of *Université de Liège* is shown in Fig. 5. It is basically a recuperative organic Rankine cycle, utilizing R1233zd(E) as working fluid. R1233zd(E) is one of the new fluids with a low GWP. Particularly, it is the recommended substitute for the fluid R245fa in ORCs and of the fluid R123 in refrigeration cycles. Thus, it is a currently significant option to investigate. Table 3 resume the working fluid characteristics.

The test bench was built using standard mass produced components from the HVAC industry, as well as from some specific industrial prototypes, such as the evaporator. The test bench consists of an evaporator, a condenser, a brazed plate recuperator (which however was by-passed during these tests), a pump and a liquid receiver. The pump

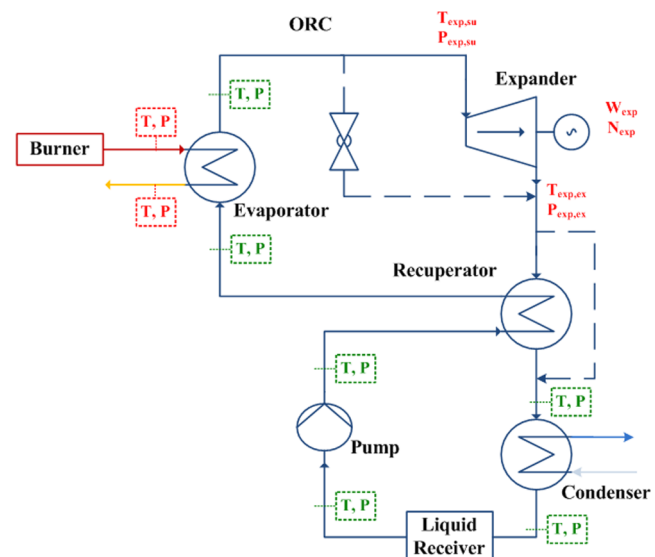


Fig. 5. Schematic of test bench (recuperative ORC).

is a Wanner Hydra-Cell piston type, which is controlled via a frequency inverter. The maximum volume flow rate and outlet discharge pressure are 30.6 l/min (at 1450 rpm) and 103 bar (at 750 rpm), respectively. The heat source is an industrial heater (burning natural gas, heating pressurized water), which allowed a maximum heat input of about 150 kW.

The thermodynamic conditions upstream and downstream the Tesla turbine were measured by installing T-type thermocouples (copper and constantan wires, very stable measuring range between  $-200$  °C and  $200$  °C, with a maximum error of  $\pm 0.5$  K) and piezoresistive pressure transducers (Keller, 30 bar, 0.25% FS). The mass flow rate was measured by using a precision Coriolis Krohne Optimass 1400Cr flow meter.

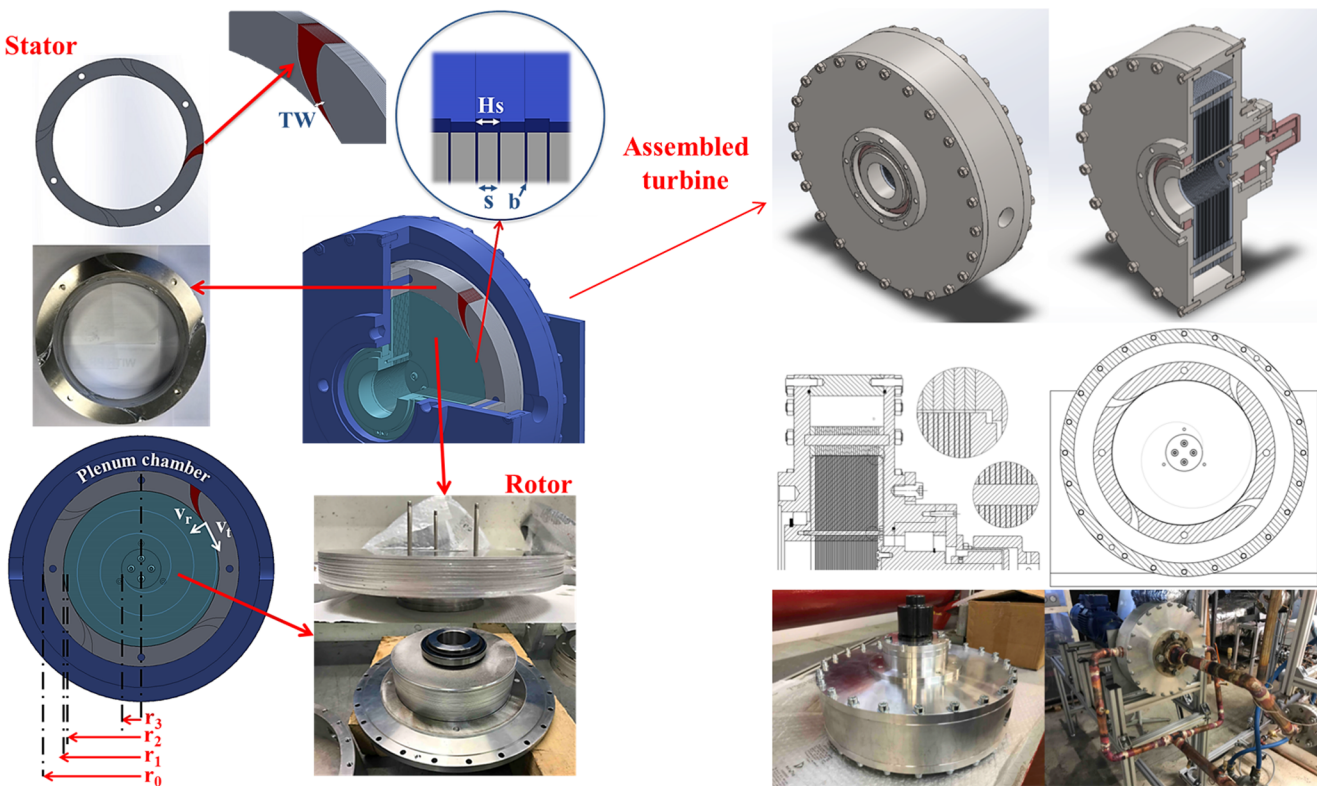


Fig. 4. Schematic of ORC Tesla turbine.

**Table 3**  
R1233zd(E) characteristics [62].

Formula	Molar mass [g/mol]	CAS number	ASHRAE classification
$C_3ClF_3H_2$	130.5	102687-65-0	A1
Critical pressure [Pa] 3,570,000	Critical Temperature [°C] 165.5	ODP 0	GWP 1

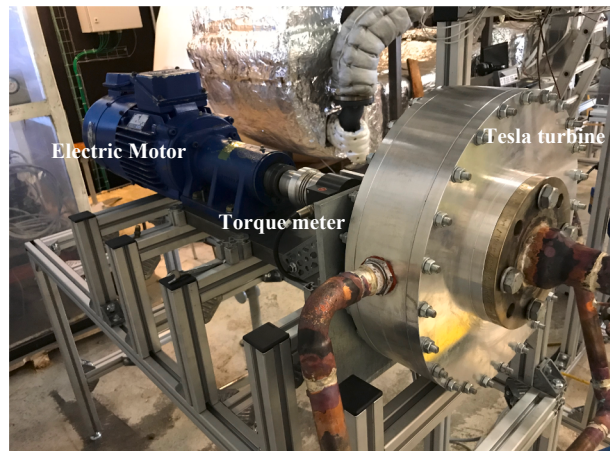


Fig. 6. Mechanical connection of ORC Tesla turbine to electric motor.

The turbine was connected to an electric motor (Perske D 6800 Mannheim 1) that controlled the rotational speed during the tests through a four-quadrant frequency inverter (ABB ACS501-01). The torque and, consequently, the power produced by the turbine was measured by a torque meter (Messtechnik DRBK, nominal torque 50 Nm, 0.5% FS) connected between the turbine and the motor through flexible couplings, as displayed in Fig. 6. All signals were acquired by a National Instruments® platform Crio-9067 (combined with NI9205, NI9208, NI9213) and processed by a software specifically developed in LabView® environment, which also allowed to control the pump and turbine rotational speeds through the inverters. The frequency of acquisition was set at 1 Hz. Table 4 summarizes the measurements ranges and accuracy of the sensors.

### 3. Experimental results

The test bench of Université de Liège allowed for the adjustment of:

- The pump mass flow rate (through a frequency inverter), which therefore allowed fixing the mass flow rate of the test bench;
- The heat input (changing the heater settings of temperature and air mass flow rate), which allowed the regulation of superheating level;
- The heat output (changing condenser water mass flow rate), which provided a control on the lower pressure of the test bench;
- The rotational speed of the turbine (through a frequency inverter), which allowed to change the related pressure drop.

The experimental campaign was conducted investigating (i) different possible refrigerant mass flow rates (0.25 – 0.36 kg/s), (ii)

different rotational speeds of the expander (1000 – 5000 rpm), (iii) different total inlet pressure (4.7 – 6.7 bar) and (iv) different superheating levels (3.2 – 46 °C). The maximum mass flow rate was imposed by the circuit, while the lower was set considering the need to provide a measurable significant power output. The maximum achievable rotational speed was 11,000 rpm - however, for the mass flow rate conditions, rotational speeds higher than 5000 rpm would lower the turbine power and efficiency. Total inlet pressure was determined by the combining effects of the heat exchanged at the heater and at the condenser.

The superheating levels were selected in order to assess the minimum and maximum levels which are present in real applications (saturated vapour or 50 °C SH).

In order to have confident temperature measurements, the turbine, the inlet and the outlet pipes were enveloped with insulating material. The explored thermodynamic conditions of the turbine for all tested points are summarized in Table 5.

Fig. 7 displays the thermodynamic representation of the test bench cycle, defining the nomenclature of the results section.

Table 5 shows six different sets of data. Each one holds the same inlet thermodynamic conditions and mass flow rate, while varying the rotational speed of the turbine.

Fig. 8 summarizes the thermodynamic conditions tested as a function of turbine expansion ratio. The explored range of expansion ratio is not very wide, but it still allows a very significant data analysis.

As can be observed from Fig. 8 (a) and (d), higher mass flow rates are directly related to higher total inlet pressure, as well as to higher expansion ratio. Nonetheless, higher expansion ratios are also obtained increasing the superheating (Fig. 8 (c)). The expansion ratio is indeed directly linked to the thermodynamic condition at the nozzle throat. High inlet pressure implies higher mass flow rate, and therefore higher pressure drop. Moreover, higher superheating level, at fixed mass flow rate (data D2 and D3 or D4 and D5) implies higher velocity at the throat section and, therefore, a higher pressure drop. High temperature implies lower densities if all the other conditions are fixed. Therefore, due to mass balance, higher velocity is achieved at the throat and, consequently, at rotor inlet.

As expected, increasing the rotational speed results into an increase of expansion ratio ( $\beta$ ), as displayed in Fig. 8 (b). The slope of the curves is almost the same for all investigated conditions. The highest expansion ratio (1.87) was achieved with 0.36 kg/s mass flow rate and super heating level of 3.35 °C, at 4000 rpm.

Fig. 9 displays the behaviour of thermodynamic power output as a function of the expansion ratio. The maximum achieved experimental thermodynamic power - defined as  $m(h_{su}-h_{ex})$  - was 906 W, with a mass flow rate of 0.299 kg/s, 44 °C superheating level at 5000 rpm rotational speed. The highest power output conditions were indeed achieved at high superheating levels (data D3 and D5), followed by high mass flow

**Table 4**  
Sensors ranges and absolute accuracies.

Quantity	Unit	Range	Maximum error (full scale)
Temperature (T-type thermocouple)	[K]	73–473	0.5
Pressure (piezoresistive pressure transducers)	[bar]	0–30	0.3
Mass flow rate (Coriolis mass flow meter)	[kg/s]	0–1	2.0 E-3
Torque	[Nm]	0–50	0.25

**Table 5**

Turbine thermodynamic characterization. Total temperature and pressure at inlet and outlet of the turbine, as well as rotational speed, torque and mass flow rate have been measured. The data have been divided in 6 datasets (D1-D6) grouping the points having the same thermodynamic conditions at turbine inlet ( $P_{00}$ , SH, mass flow rate) but different turbine rotational speed.

Dataset Nomenclature	Points	Rotational Speed [rpm]	Torque [Nm]	Mass flow rate [kg/s]	$T_{00}$ [°C]	$P_{00}$ [Pa]	$T_{03}$ [°C]	$P_{03}$ [Pa]
D1	1	2000	1.25	0.3568	86.84	635,633	80.40	404,818
	2	2500	1.09	0.3566	87.13	644,701	80.29	405,224
	3	3000	0.92	0.3564	87.08	653,135	80.01	404,749
	4	3500	0.73	0.3565	87.19	664,151	79.86	406,106
	5	4000	0.58	0.3567	87.11	673,920	79.59	403,996
D2	6	1500	1.01	0.2541	73.42	473,535	68.41	311,123
	7	1750	0.95	0.2541	73.14	476,446	67.84	311,310
	8	2000	0.89	0.2541	73.25	479,870	67.69	312,341
	9	2250	0.83	0.2540	73.04	482,052	67.55	311,048
	10	2500	0.75	0.2538	72.98	486,119	67.37	311,947
	11	2750	0.70	0.2539	72.74	489,369	67.03	311,867
D3	12	3000	0.64	0.2539	72.66	493,133	66.74	312,004
	13	3500	0.60	0.2532	108.10	518,962	101.48	321,518
	14	3250	0.63	0.2531	108.56	515,830	102.46	321,805
	15	3000	0.69	0.2530	108.39	512,314	102.59	322,445
	16	2750	0.74	0.2530	108.32	508,854	102.83	322,654
	17	2500	0.78	0.2529	107.60	505,954	102.43	323,276
D4	18	2250	0.82	0.2530	107.01	501,261	101.71	322,265
	19	1500	1.26	0.3009	76.38	518,794	76.38	319,829
	20	1750	1.20	0.3009	76.32	521,596	76.32	318,935
	21	2000	1.12	0.3009	74.98	523,252	74.98	318,879
	22	2250	1.05	0.3009	75.31	527,202	75.31	317,822
	23	2500	0.97	0.3008	74.84	530,978	74.84	318,973
D5	24	2750	0.91	0.3007	75.44	536,251	75.44	319,886
	25	3000	0.84	0.3008	75.00	539,307	75.00	318,254
	26	3250	0.78	0.3007	74.96	543,242	74.96	315,476
	27	3500	0.70	0.3006	75.42	547,545	75.42	316,069
	28	3750	0.64	0.3008	74.59	550,591	74.59	315,065
	29	5000	0.60	0.2993	120.26	598,959	112.95	325,804
D6	30	4500	0.76	0.2994	120.13	588,417	113.41	326,683
	31	4000	0.89	0.2993	120.20	577,387	113.78	326,823
	32	3500	0.99	0.2992	119.92	569,026	113.76	327,326
	33	3000	1.10	0.2992	119.76	561,617	113.80	328,327
D6	34	1000	1.78	0.3651	78.59	578,933	72.42	343,426
	35	1500	1.65	0.3646	79.28	584,299	72.44	340,593
	36	2000	1.49	0.3642	79.88	589,228	72.68	339,009
	37	2500	1.33	0.3640	79.93	596,259	72.46	338,396
	38	3000	1.15	0.3641	79.81	605,988	71.92	338,649
	39	3500	1.01	0.3635	82.04	616,757	73.83	338,801
	40	4000	0.84	0.3640	81.26	624,814	72.78	333,418

rate conditions (data D1 and D6). Furthermore, as expected, the thermodynamic power increases with the expansion ratio. It is very interesting to notice that the same expansion ratio can be obtained either at high super heating level or mass flow rate, but the power output is higher in the former case. For example, at about 1.8 expansion ratio, it can be observed from Fig. 9 that the turbine produces nearly 18% more

power with 0.299 kg/s mass flow rate, a super heating level of 44.6 °C and a rotational speed of 4500 rpm compared to the case with 0.364 kg/s mass flow rate, a 3.2 °C super heating level and a rotational speed of 3500 rpm. This is due to a couple of significant effects: (i) the higher available expansion work per unite mass (higher inlet temperature at about the same inlet pressure), that allows an increase in the available thermodynamic power; the (ii) a better match between rotational speed and tangential velocity is achieved, allowing a better power conversion. This effect has been deeply addressed in [63], where it is shown how optimal efficiencies (and consequently power conversion) are achieved when the inlet tangential velocity ratio ( $\frac{v_2}{u_2}$ ) is equal or close to 1.

Fig. 10 shows the thermodynamic power output as a function of expansion ratio and rotational speed. High expansion ratios and rotational speeds favour power production, while low rotational speeds and expansion ratios hinder the power production.

Differently from the experimental thermodynamic power, the maximum achieved shaft power output was 371 W at two different conditions: in the first case, it was obtained with 0.299 kg/s mass flow rate and 45.5 °C superheating level, at 4000 rpm rotational speed; in the second case, it was achieved with 0.365 kg/s mass flow rate, 4.65 °C super heating level at 3500 rpm rotational speed.

As can be easily noticed from Figs. 9 and 11, the measured shaft power output shows a different behaviour compared to the thermodynamic one. The thermodynamic power output is monotonically

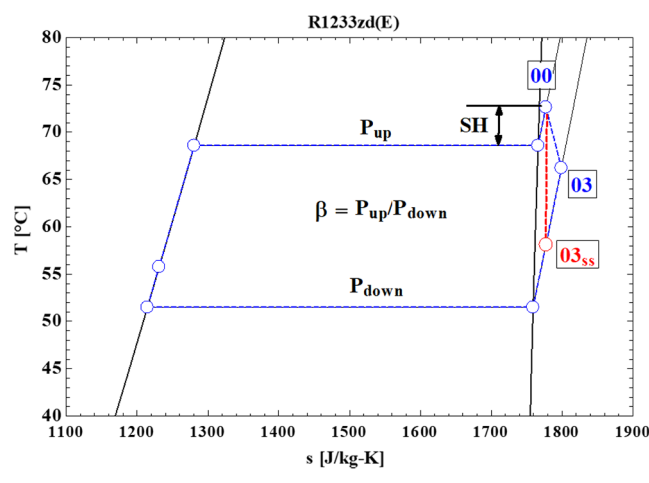


Fig. 7. Thermodynamic representation (T-s diagram) of test bench cycle.

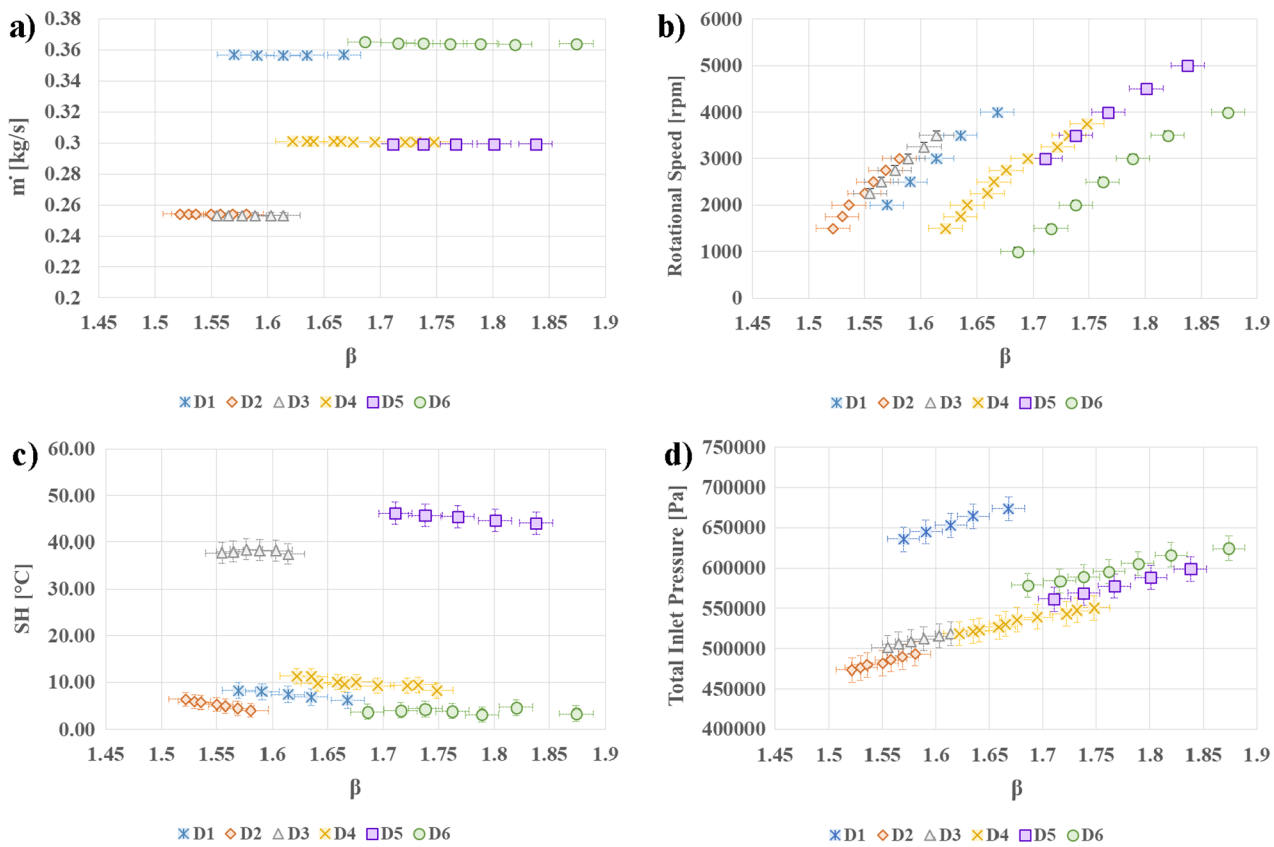


Fig. 8. Experimental data: mass flow rate a), rotational speed b), superheating level c) and total turbine inlet pressure d) as a function of expansion ratio.

increasing with expansion ratio and rotational speed, while the shaft power output shows a maximization point.

The behaviour of shaft power output can be better understood when analysing Fig. 12, where it is reported as a contour plot vs. expansion ratio and rotational speed. The former increases with the turbine rotational speed, but it also directly increases the mechanical losses due to the bearings, as well as the friction losses due to the electromagnetic coupling.

On average, a 50% mechanical efficiency (ratio of shaft power over thermodynamic power) was achieved that is a really low value, mostly attributable to the improper alignment of the magnetic coupling, which is responsible for a very high increase of the mechanical friction losses.

The maximum achieved experimental adiabatic efficiency ( $\eta_{ad} = \frac{h_{00} - h_{03}}{h_{00} - h_{03ss}}$ ) was 30% with 0.253 kg/s mass flow rate, 37.5 °C super heating level and 3500 rpm rotational speed.

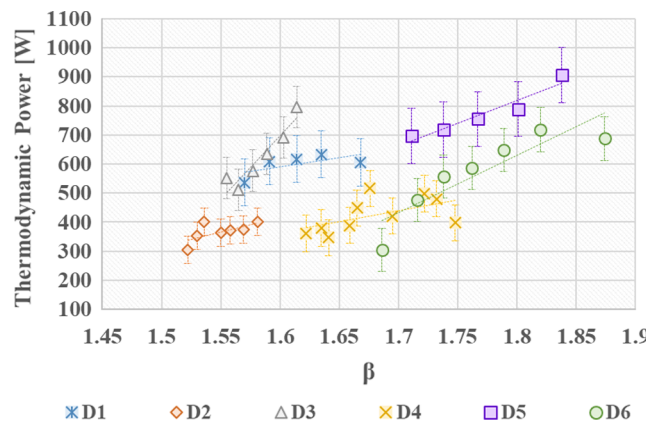


Fig. 9. Experimental thermodynamic power output vs. expansion ratio.

The highest adiabatic efficiency values are directly related to the thermodynamic power output; nonetheless, as expected for a Tesla turbine, higher efficiencies are achieved at low mass flow rates. Indeed, if Figs. 9 and 13 are examined together, it clearly appears that there is a direct relationship between power production and adiabatic efficiency. However, as above remarked, the low mass flow rates conditions (data groups D2 and D3) achieve higher efficiencies compared to the high mass flow rates ones (data groups D1 and D6). On the whole, an average 17% adiabatic efficiency was measured for this expander, with higher values at low mass flow rate conditions. Fig. 14 shows the experimentally interpolated contour plot of the adiabatic efficiency. Highest efficiencies are achieved at low pressure ratios (therefore low mass flow rates) and high rotational speeds, which correspond to a better match between inlet tangential velocity and rotational speed (so to a better power conversion).

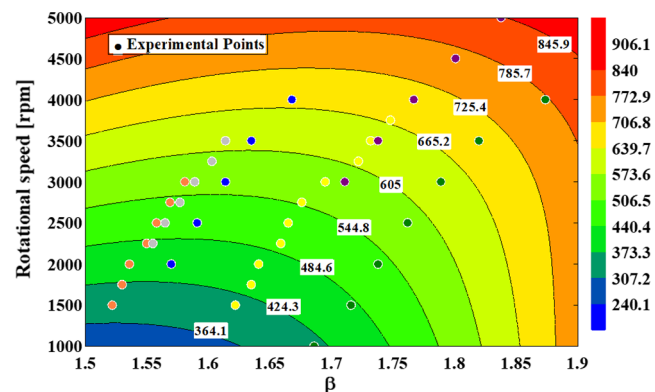


Fig. 10. Experimental interpolated contour plot of thermodynamic power output as a function of expansion ratio and rotational speed. Bi-quadratic interpolation method has been applied.

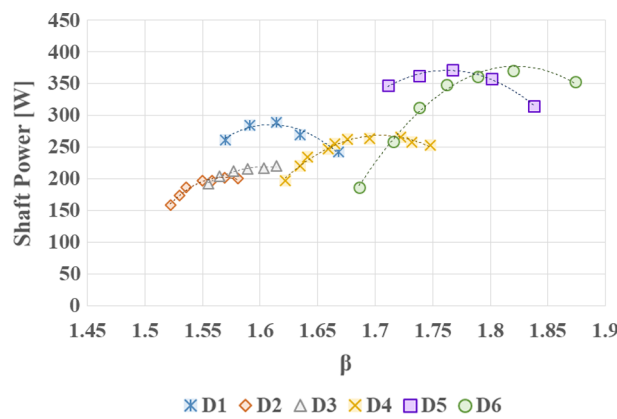


Fig. 11. Experimental shaft power as function of expansion ratio.

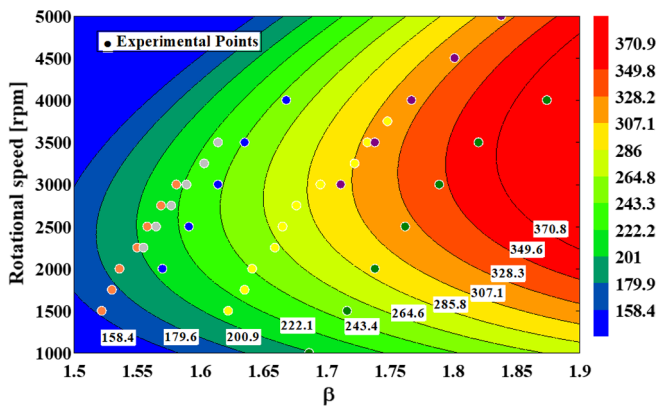


Fig. 12. Experimental interpolated contour plot of shaft power as function of expansion ratio and rotational speed. Bi-quadratic interpolation method has been applied.

The shaft efficiency ( $\eta_{\text{shaft}} = \frac{\text{work}_{\text{shaft}}}{h_{00} - h_{03ss}}$ ) - Fig. 15-, on the other hand, is directly related to the obtained shaft power. Therefore, the highest shaft efficiency condition corresponds to that of maximum power output, which is at 0.299 kg/s mass flow rate, 45.5 °C super heating level and 4000 rpm rotational speed. Under these conditions, 9.62% shaft efficiency is achieved. Nonetheless, there is still an influence of mass flow rate; at low values, the efficiency is still relatively high, even at lower power output.

On the whole, an average shaft efficiency of 8.2% was measured for this expander, with higher values at low mass flow rate and high power output conditions. Fig. 16 displays the experimentally interpolated contour plot of the shaft efficiency. Optimal values are achieved at

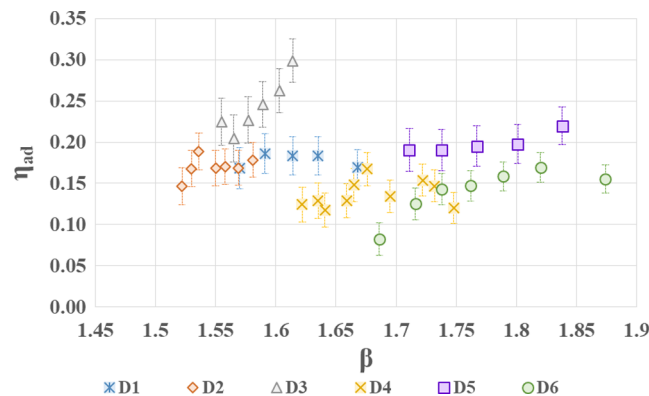


Fig. 13. Experimental adiabatic efficiency of the Tesla turbine prototype vs. expansion ratio.

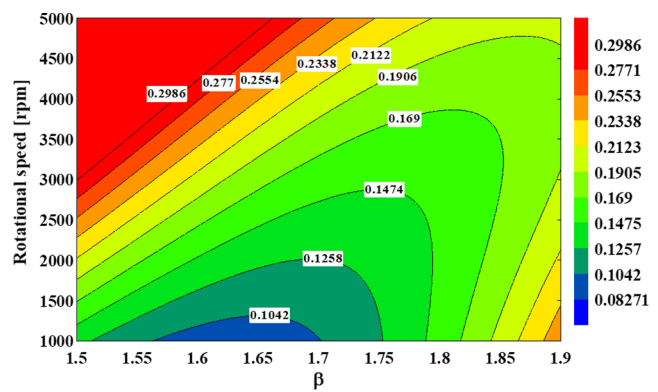


Fig. 14. Experimental interpolated contour plot of adiabatic efficiency as function of expansion ratio and rotational speed. Bi-quadratic interpolation method has been applied.

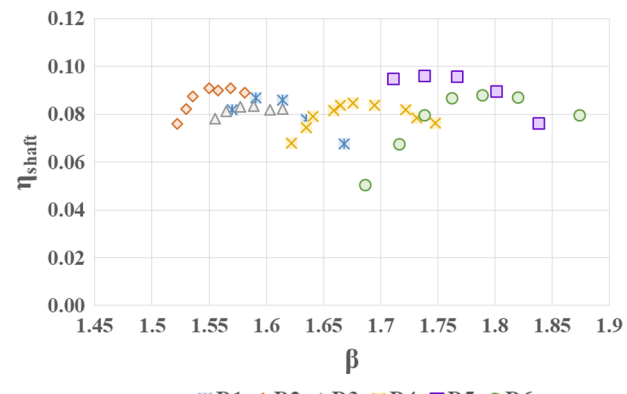


Fig. 15. Experimental shaft efficiency as function of expansion ratio.

3000 rpm with moderate pressure ratios.

As can be noticed from the very large difference between adiabatic and shaft efficiency, as well as from the values of organic efficiency, the mechanical power losses of the turbine are quite high.

As above remarked, the main reason of such discrepancy is given by the not proper alignment of the magnetic coupling of the turbine during the experimental campaign. Fig. 17 summarizes the experimental power losses of the turbine, compared to the predicted bearing losses and the sum of bearings losses and friction losses due to the contact of the electromagnetic coupling. For the estimation of the bearings mechanical losses, the model provided by the manufacturer was applied [64]. The estimated bearings losses are expressed by Eq. (1).

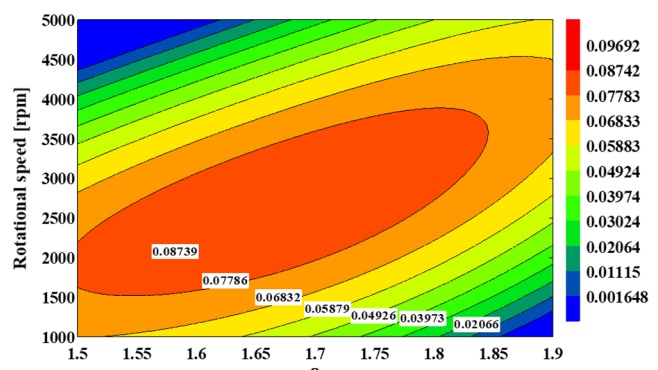


Fig. 16. Experimental interpolated contour plot of shaft efficiency as function of expansion ratio and rotational speed. Bi-quadratic interpolation method has been applied.

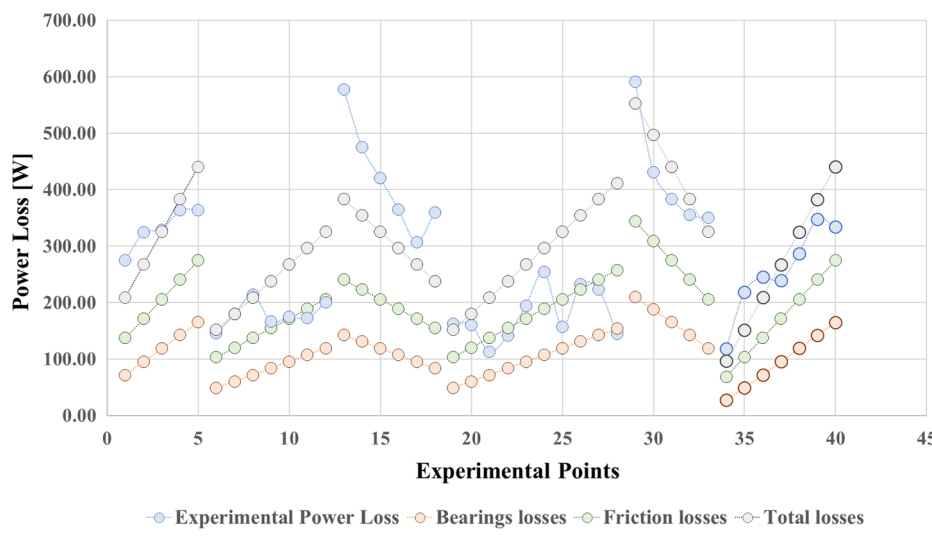


Fig. 17. Mechanical losses of ORC Tesla turbine.

$$P_{\text{loss}} = \omega \cdot M_{\text{loss}}$$

Where  $M_{\text{loss}}$  is the bearings frictional torque, which takes into account of the rolling and sliding contributions. The rolling frictional moment ( $M_r$ ) can be calculated through Eq. (2), while the sliding frictional moment ( $M_s$ ) can be computed through Eq. (3).

$$M_r = \phi_{ish} \phi_{rs} G_r (\nu \cdot n)^{0.6}$$

$$M_s = G_s \cdot \mu_s$$

Where  $\phi_{ish}$  is the inlet shear heating reduction factor,  $\phi_{rs}$  is the kinematic replenishment/starvation reduction factor,  $G_r$  is a variable depending on bearing type, diameter and load,  $n$  is the rotational speed [rpm],  $\nu$  is the operating viscosity of the oil (or grease) [ $\text{mm}^2/\text{s}$ ],  $G_s$  is a variable depending on bearing type, diameter and load and  $\mu_s$  is the sliding friction coefficient [64].

For the estimation of the losses derived by the contact of the electromagnetic coupling, the model of friction losses on a carrier pin was applied. The estimated pin friction losses are expressed by Eq. (4).

$$P_{\text{loss,pin}} = \omega \cdot M_r$$

Where  $M_r$  is the frictional torque, which is the friction force time the radius of electromagnetic coupling, with a coefficient  $f = 0.15$  for steel over steel materials [65].

#### 4. Comparison between experimental results and in-house code

Not only mechanical but also fluid dynamic losses need to be added to the original developed 2-D in house code [56–59].

The 2-D model for the assessment of the fluid dynamics of the Tesla turbine was developed in EES environment [66]. The model was aimed at the design of the complete turbine, therefore considering not only the rotor, but also the stator and the gap in between the two parts [56,57]. The model takes into account a viscous, real, compressible, steady state flow; all thermodynamic properties are obtained through internal EES fluid properties libraries, defined through local variables (usually temperature and pressure). Body viscous forces are assumed negligible in comparison to the viscous forces along the radial and tangential directions. These assumptions lead to a simplified formulation of the Navier-Stokes equations in cylindrical coordinates.

The present model was solved assuming a parabolic axial velocity profile, corresponding to fully developed laminar flow [57], and neglecting body viscous forces (considered marginal compared to the viscous forces along the radial and tangential directions).

The reduced  $\theta$ - and  $r$ -momentum equations were obtained (Eqs. (5)

and (6)) and defined in the EES software by using a step forward method (centred finite difference method).

$$\frac{\partial w_\theta}{\partial r} = -\frac{10}{a} \Omega - \left( \frac{60\nu}{w_r ab^2} + \frac{1}{r} \right) w_\theta \quad (5)$$

$$\frac{1}{\rho} \frac{dp}{dr} = -w_r \frac{\partial w_r}{\partial r} \frac{a^2}{30} + \Omega^2 r + 2\Omega w_\theta \frac{a}{6} + \frac{w_\theta^2}{r} \frac{a^2}{30} - \nu w_r \frac{2a}{b^2} \quad (6)$$

The  $a$  coefficient is adjusted to account for transitional conditions occurring in the entry region [59].

The code did not initially consider flow blockage due to the throttling effects of disks edges, windage between end disks and the case and pumping losses. If these are not taken into account, the power output predicted by the 2D calculation model is much higher than the experimental value measured in this campaign. This is physically due to the not proper sealing of the flow between rotor and casing: this effect is enhanced at relatively high expansion ratios (e.g. 2–4), as happens in case of ORC Tesla expanders, whereas it is more or less negligible in case of modest expansion ratios, as in the case of working with air where the expander manages only few kPa pressure drops. As shown in Fig. 18, the size of the gap between end rotors and casing and the width between the disks channels are of the same order of magnitude (tenths of millimetre), thus giving no preferential path to the flow. Consequently, the model has been upgraded to include the blockage, windage & pumping losses.

Fig. 19 shows the thermodynamic effect of blockage, windage and pumping losses on the T-s diagram. The fluid first undergoes a pressure drop due to the abrupt enlargement losses derived from exiting the stator and entering the gap, then a further pressure loss comes from the restriction at the gap-rotor channels inlet passage. The effects of blockage, windage and pumping losses are then taken into account. In particular, these losses increase the temperature at rotor inlet, besides increasing the entropy, which results in a reduction of the available work.

Therefore, in order to improve the Tesla turbine calculation code, a model including the effects of blockage, windage and pumping losses was added [67].

The estimated windage losses are expressed by Eq. (7)

$$P_w = 0.1 \cdot \frac{\pi \cdot d_2 \cdot H \cdot \varepsilon}{2} \cdot \rho \cdot u_2^3 \quad (7)$$

Where  $H$  is the total thickness of the rotor disks package (0.0008\*30 [m]) and  $\varepsilon$  is the partialization degree, defined as  $\varepsilon = 1 - \frac{4 \cdot A_{out, nozzle}}{A_{in, rotor}}$

The blockage losses are expressed by Eq. (8):

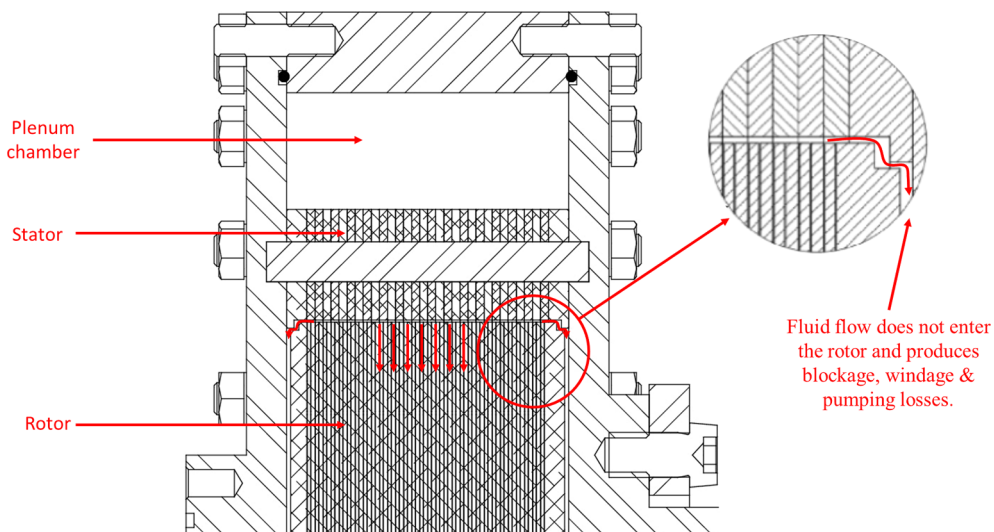


Fig. 18. Representation of fluid path within the turbine producing blockage, windage & pumping losses.

$$P_{pt} = 0.15 \cdot \frac{v_{1s}}{u} \cdot \dot{m} \cdot \frac{(r_2 - r_3)}{d_2} \cdot \frac{u^2}{\epsilon} \quad (8)$$

Where  $v_{1s}$  is the isentropic absolute velocity at stator outlet.

The pumping losses are expressed by Eq. (9)

$$P_{pp} = 4 \cdot C_M \cdot \rho \cdot d_2^2 \cdot u^3 \quad (9)$$

Where  $C_M$  is a coefficient depending on Reynolds number, expressed as  $C_M = 0.003 \cdot Re^{-2}$  [67].

This model was originally developed for partial admission steam turbines, and therefore it takes into account of experimental coefficients (0.1 for windage losses and 0.15 for blockage losses), which do not proper fit organic fluids.

In order to readapt the coefficients to the current case of Tesla expander working with organic fluids in place of steam for which the above correlations were derived, it was decided to try interpolating the ratio between the actual measured power output and the value calculated by the EES 2D model, including blockage, windage and pumping losses. The experimental fit coefficient was interpolated as a function of Mach number and temperature at the stator outlet, after having included the enlargement losses.

The interpolated equation is expressed by Eq. (10). In spite of the not very high amount of available experimental data, which does not allow for an accurate experimental fitting of the whole dataset, the procedure and the interpolated coefficient still produces a reliable

prediction. Fig. 20 shows the expression of the experimental interpolation surface, as a function of Mach number and temperature.

$$C_{exp} = -31.08 - 0.023 - 31.08 \cdot T + 100.8 * Ma + 0.0199 \cdot T \cdot Ma - 77.04 \cdot Ma^2 \quad (10)$$

Finally, the upgraded 2D EES in-house code, including the above models to account for the blockage, windage and pumping losses and with the tuned experimental coefficient, was applied and the results are displayed in Figs. 21 and 22.

In this way, the 2D EES code properly describes the behaviour of both thermodynamic power output and adiabatic efficiency, with a satisfactory agreement level between calculated and measured data. The mean absolute deviation between experimental power and efficiency and the corresponding simulated values is about 8%; the Pearson coefficient for the power is 0.95 and for the efficiency is 0.92. The coefficient of correlation for the power is 0.89 and for efficiency is 0.85.

## 5. Conclusions

An experimental investigation campaign on an Organic Rankine Cycle Tesla turbine was carried out. This campaign is the first documented with organic fluids, and therefore it allows a proof of concept of the technology. A pivotal point of this research is the comparison between experimental and numerical results, which resulted in fair agreement.

The key achievements are summarized as follows:

- An experimental test campaign was conducted with Organic Rankine Cycle Tesla turbine, with several mass flow rates of R1233zd(E) at various rotational speeds and total inlet conditions. The maximum achieved adiabatic efficiency was 30%, with 0.253 kg/s mass flow rate, 37.5 °C super heating level at 3500 rpm rotational speed; while the maximum achieved experimental thermodynamic power output was 906 W, with 0.299 kg/s mass flow rate, 44 °C super heating level at 5000 rpm rotational speed.
- The maximum achieved shaft efficiency of the Organic Rankine Cycle Tesla turbine was 9.62%, with 0.299 kg/s mass flow rate, 45.5 °C super heating level at 4000 rpm rotational speed; while the maximum achieved experimental shaft power output was 371 W under two different conditions: (i) at 0.299 kg/s mass flow rate, 45.5 °C super heating level at 4000 rpm rotational speed; (ii) at 0.365 kg/s mass flow rate, 4.65 °C super heating level at 3500 rpm rotational speed.
- The mechanical efficiency of the Organic Rankine Cycle Tesla

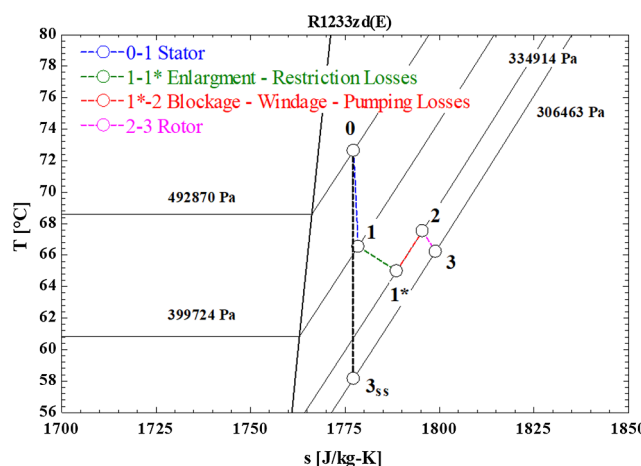
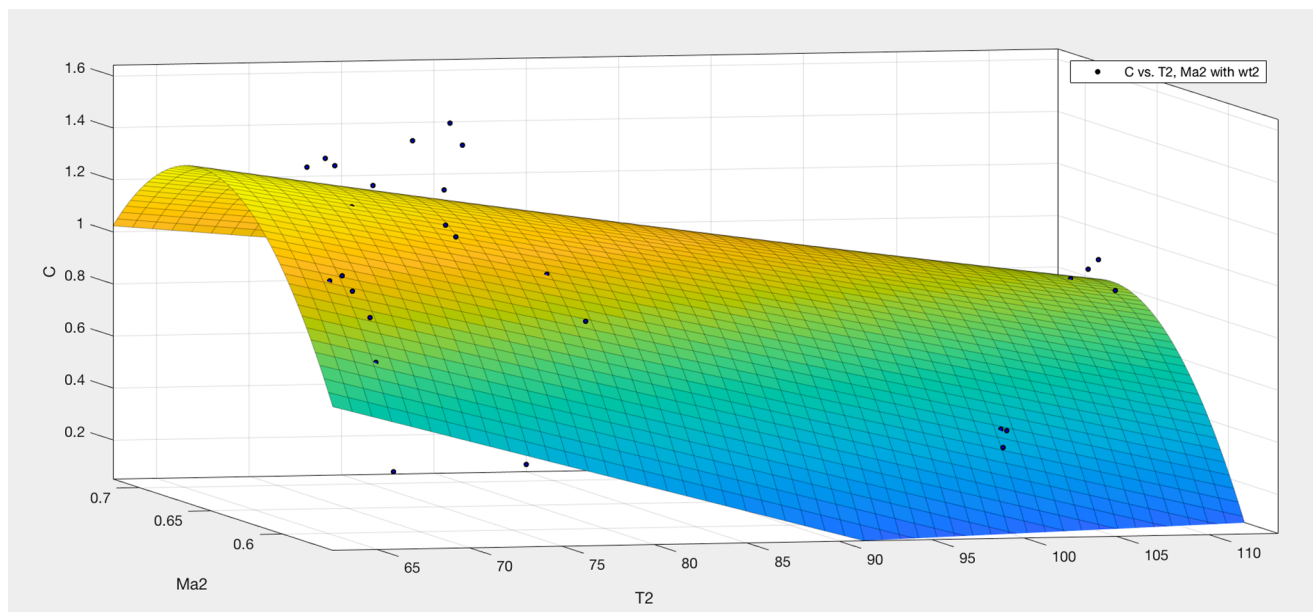
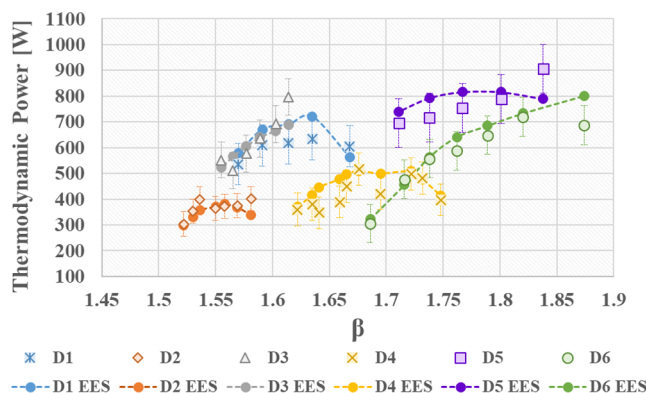


Fig. 19. Thermodynamic representation of losses occurring in stator-rotor gap.



**Fig. 20.** Interpolation surface of experimental constant.



**Fig. 21.** Experimental data and numerical prediction of thermodynamic power vs. expansion ratio.

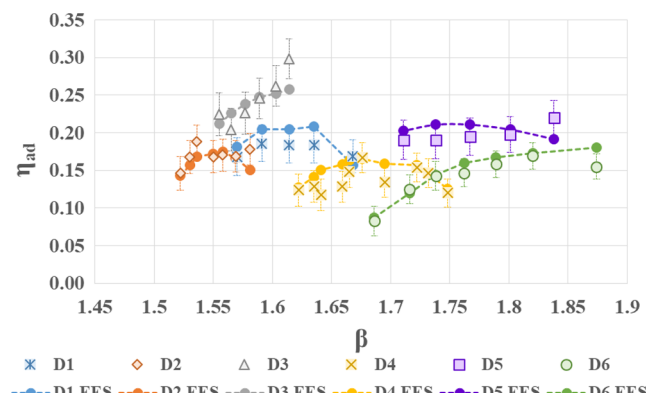


**Fig. 22.** Experimental data and numerical prediction of adiabatic efficiency vs. expansion ratio.

prototype (including generator and torque meter losses) was estimated at 50%, which is a really low value, mostly influenced by the non-correct alignment of the magnetic coupling, which brought a really high increase of mechanical losses due to friction.

- By modifying the 2D EES in-house code such as to account for flow blockage, windage and pumping losses, also including the

experimental constant coefficient, it properly described the behaviour of both thermodynamic power and adiabatic efficiency, with numerical prediction always within the uncertainty of the measured data. Indeed, the mean absolute deviation between experimental and computed data was of 8%, both for power and efficiency. It is a noticeable achievement, allowing the physical validation of the improved 2D model which takes into account of blockage, windage and pumping losses, that become relevant at relatively high expansion ratios (2–4), at which the throttling effect of the disk rotors is exalted. This effect becomes less relevant and progressively negligible at reduced values of expansion ratios. In this way, the developed 2D model becomes a very important tool in designer's hands, allowing the determination of the optimal disks gap at given expansion conditions.

#### Declaration of Competing Interest

The authors declare that they have no known competing financial interests or personal relationships that could have appeared to influence the work reported in this paper.

#### References

- [1] S. Quoilin, S. Declaye, B.F. Tchancle, V. Lemort, Thermo-economic optimization of waste heat recovery Organic Rankine Cycles, *Appl. Therm. Eng.* 31 (2011) 2885–2893.
- [2] T. Sung, K.C. Kim, Thermodynamic analysis of a novel dual-loop organic Rankine cycle for engine waste heat and LNG cold, *Appl. Therm. Eng.* 100 (2016) 1031–1041.
- [3] G. Qiu, Selection of working fluids for micro-CHP systems with ORC, *Renew. Energy* 48 (2012) 565–570.
- [4] M. Santos, J. André, E. Costa, R. Mendes, J. Ribeiro, Design strategy for component and working fluids selection in a domestic micro-CHP ORC boiler, *Appl. Therm. Eng.* (2020) 169.
- [5] K. Braimakis, S. Karella, Integrated thermo-economic optimization of standards and regenerative ORC for different heat source types and capacities, *Energy* (2017) 570–598.
- [6] S. Lecompte, H. Huisseune, M. Van Den Broek, B. Vanslambrouck, M. De Paepe, Review of Organic Rankine Cycle (ORC) architectures for waste heat recovery, *Renew. Sustain. Energy Rev.* 47 (2015) 448–461.
- [7] G. Qiu, H. Liu, S. Riffat, Expanders for micro-CHP systems with organic Rankine cycle, *Appl. Therm. Eng.* 31 (2011) 3301–3307.
- [8] D. Fiaschi, G. Innocenti, G. Manfrida, F. Maraschillo, Design of micro radial turboexpanders for ORC power cycles: From 0D to 3D, *Appl. Therm. Eng.* 99 (2016) 402–410.
- [9] Gianluca Carraro, Sergio Rech, Andrea Lazzaretto, Giuseppe Toniato, Piero Danieli,

- Dynamic simulation and experiments of a low-cost small ORC unit for market applications, *Energy Convers. Manage.* 197 (2019) 111863, <https://doi.org/10.1016/j.enconman.2019.111863>.
- [10] B. Peris, J. Navarro-Esbrí, F. Moles, R. Collado, A. Mota-Babiloni, Performance evaluation of an Organic Rankine Cycle (ORC) for power applications from low grade heat sources, *Appl. Therm. Eng.* 75 (2015) 763–769.
- [11] D. Ziviani, A. Beyene, M. Venturini, Design, Analysis and Optimization of a Micro-CHP System Based on Organic Rankine Cycle for Ultralow Grade Thermal Energy Recovery, *J. Energy Resour. Technol.* 136 (2013) 1.
- [12] P. Bombarda, C. Invernizzi, C. Pietra, Heat recovery from diesel engines: a thermodynamic comparison between Kalina and ORC cycles, *Appl. Therm. Eng.* 30 (2009) 212–219.
- [13] M.M. Rashidi, N. Galanis, F. Nazari, A.B. Parsa, L. Shamekhi, Parametric analysis and optimization of regenerative Clausius and organic Rankine cycles with two feed water heaters using artificial bees colony and artificial neural network, *Energy*, 36 (9) (2011) 5728–5740.
- [14] A. Habibzadeh, M.M. Rashidi, Thermodynamic analysis of different working fluids used in organic Rankine cycle for recovering waster heat from GT\_MHR, *J. Eng. Sci. Technol.* 11 (1) (2016) 121–135.
- [15] J. Bao, L. Zhao, A review of working fluid and expander selections for organic Rankine cycle, *Renew. Sustain. Energy Rev.* 24 (2013) 325–342.
- [16] L. Talluri, G. Lombardi, Simulation and Design Tool for ORC Axial Turbine stage, *Energy Procedia* 129 (2017) 277–284.
- [17] B. Vanslambrouck, I. Vankeirsbilck, S. Gusev, Turn waste heat into electricity by using an Organic Rankine Cycle, 2nd European Conference on Polygeneration, Tarragona (Spain) 2011.
- [18] G. Zywnica, T.Z. Kaczmarczyk, E. Ihnatowicz, A review of expanders for power generation in small-scale organic Rankine cycle systems: Performance and operational aspects, *Proc. Inst. Mech. Eng., Part A: J. Power Energy* 230 (2016) 669–684.
- [19] P. Song, M. Wei, L. Shi, S.N. Danish, C. Ma, A review of scroll expanders for organic Rankine cycle systems, *Appl. Therm. Eng.* 75 (2015) 54–64.
- [20] S. Quoilin, Sustainable energy conversion through the use of Organic Ranke Cycles for waste heat recovery and solar application, Doctor dissertation University of Liège, 2011.
- [21] A.P. Weiss, T. Popp, G. Zinn, M. Preissinger, D. Bruggemann, A micro-turbine-generator-construction-kit (MTG-c-kit) for small scale waste heat recovery ORC-Plants, *Energy* 181 (2019) 51–55.
- [22] S.H. Hang, Design and experimental study of ORC (organic Rankine cycle) and radial turbine using R245fa working fluid, *Energy* 41 (2012) 514–524.
- [23] O. Dumont, A. Parthoen, R. Dickes, V. Lemort, Experimental investigation and optimal performance assessment of four volumetric expanders (scroll, screw, piston and roots) tested in a small-scale organic Rankine cycle system, *Energy* 165 (2018) 1119–1127.
- [24] A. Mandal, S. Saha, Performance analysis of a centimetre scale Tesla turbine for micro-air vehicles, *2017 International conference of Electronics, Communication and Aerospace Technology (ICECA), Coimbatore* (2017) 62–67.
- [25] V. Lemort, I. Bell, E. Groll, J. Braun, Analysis of Liquid-Flooded Expansion Using a Scroll Expander (2019).
- [26] S. Quoilin, V. Lemort, J. Lebrun, Experimental study and modelling of an Organic Rankine Cycle using scroll expander, *Appl. Energy* 87 (2010) 1260–1268.
- [27] Z. Wu, D. Pan, N. Gao, T. Zhu, F. Xie, Experimental testing and numerical simulation of scroll expander in a small scale organic Rankine cycle system, *Appl. Therm. Eng.* 87 (2015) 529–537.
- [28] S. Declaye, S. Quoilin, L. Guillaume, V. Lemort, Experimental study on an open-drive scroll expander integrated into an ORC (Organic Rankine Cycle) system with R245fa as working fluid, *Energy* 55 (2013) 173–183.
- [29] B. Lei, W. Wang, Y.T. Wu, C.F. Ma, J.F. Wang, L. Zhang, C. Li, Y.K. Zhao, R.P. Zhi, Development and experimental study on a single screw expander integrated into an Organic Rankine Cycle, *Energy* 116 (2016) 43–52.
- [30] D. Ziviani, S. Gusev, S. Lecompte, E.A. Groll, J.E. Braun, W.T. Horton, M. Van Den Broek, M. De Peape, Characterizing the performance of a single-screw expander in small-scale organic Rankine cycle for waste heat recovery, *Appl. Energy* 181 (2016) 155–170.
- [31] M. Bianchi, L. Branchini, N. Casari, A. De Pascale, F. Melino, S. Ottaviano, M. Pinelli, P.R. Spina, A. Suman, Experimental analysis of a micro-ORC driven by piston expander for low-grade heat recovery, *Appl. Therm. Eng.* 148 (2019) 1278–1291.
- [32] N. Zheng, L. Zhao, X.D. Wang, Y.T. Tan, Experimental verification of a rolling-piston expander that applied for low-temperature Organic Rankine Cycle, *Appl. Energy* 112 (2013) 1265–1274.
- [33] V. Lemort, A. Legros, Positive displacement expanders for Organic Rankine Cycle systems, in: M. Macchi, M. Astolfi (Eds.), *Organic Rankine Cycle (ORC) Power Systems, Technologies and Applications*, 1st Edition, Woodhead Publishing, Elsevier (2016).
- [34] J.H. Armstrong, An Investigation of the Performance of a Modified Tesla Turbine, M.Sc Thesis Georgia Institute of Technology, 1952.
- [35] W. Rice, An analytical and experimental investigation of multiple-disk turbines, *ASME J. Eng. Power* 87 (1965) 29–36.
- [36] R. Steidel, H. Weiss, Performance test of a bladeless turbine for geothermal applications, Technical Report Report No. UCID-17068, California Univ., Livermore (USA), Lawrence Livermore Lab., (1976).
- [37] V.P. Carey, Assessment of Tesla Turbine Performance for Small Scale Rankine Combined Heat and Power Systems, *J. Eng. Gas Turbines Power* 132 (2010) 1–8.
- [38] Tesla N., Turbine, U.S. Patent No. 1 061 206, 1913.
- [39] A.B. Leaman, The design, construction and investigation of a Tesla turbine, M.Sc. Thesis, University of Maryland, (1950).
- [40] J.S. Allen, A model for fluid between parallel, co-rotating annular disks, M.Sc Thesis University of Dayton, Ohio, 1990.
- [41] S. Sengupta, A. Guha, Analytical and computational solutions for three-dimensional flow-field and relative pathlines for the rotating flow in a Tesla disc turbine, *Comput. Fluids* 88 (2013) 344–353.
- [42] A. Guha, S. Sengupta, The fluid dynamics of work transfer in the non-uniform viscous rotating flow within a Tesla disc turbomachine, *Phys. Fluids* 26 (2014) 1–27.
- [43] V.D. Romanin, V.G. Krishnan, V.P. Carey, M.M. Maharbiz, Experimental and analytical study of a sub-watt scale Tesla turbine performance, *Proceedings of the ASME 2012 International Mechanical Engineering Congress & Exposition*, (2012).
- [44] C. Schosser, T. Fuchs, R. Hain, S. Lecheler, C. Kahler, Three-dimensional particle tracking velocimetry in a Tesla turbine rotor using a non-intrusive calibration method, in: 18th International Symposium on the Application of Laser and Imaging Techniques to Fluid Mechanics, Lisbon, (2016).
- [45] C. Schosser, S. Lecheler, M. Pfitzner, Analytical and numerical solutions of the rotor flow in Tesla turbines, *Periodica Polytechnica Mech. Eng.* 61 (2017) 12–22.
- [46] K. Rusin, W. Wroblewski, S. Rulik, The evaluation of numerical methods for determining the efficiency of Tesla turbine operation, *J. Mech. Sci. Technol.* 32 (2018) 5711–5721.
- [47] T.W. Choon, A.A. Rahman, F.S. Jer, L.E. Aik, Optimization of Tesla turbine using Computational Fluid Dynamics approach, in: *IEEE Symposium on Industrial Electronics and Applications (ISIEA2011)*, (2011).
- [48] E. Lemma, R.T. Deam, D. Toncich, R. Collins, Characterisation of a small viscous flow turbine, *Exp. Therm. Fluid Sci.* 33 (2008) 96–105.
- [49] A.L. Neckel, M. Godinho, Influence of geometry on the efficiency of convergent-divergent nozzles applied to Tesla turbines, *Exp. Therm. Fluid Sci.* 62 (2015) 131–140.
- [50] A. Renuke, A. Traverso, M. Pascenti, Experimental Campaign Tests on a Tesla Micro-expander, in: Sustainable PolyEnergy generation and Harvesting Conference and Exhibition – SUPEHR19, September 4th-6th, Savona, Italy.
- [51] A. Renuke, A. Traverso, M. Pascenti, Experimental and computational investigation of Tesla Air Micro-Expanders, *International Gas Turbine Congress (IGTC)*, (2019).
- [52] P. Lampart, L. Jedrzejewski, Investigations of aerodynamics of Tesla bladeless microturbines, *J. Theoret. Appl. Mech.* 49 (2) (2011) 477–499.
- [53] J. Song, C.W. Gu, X.S. Li, Performance estimation of Tesla turbine applied in small scale Organic Rankine Cycle (ORC) system, *Appl. Therm. Eng.* 110 (2017) 318–326.
- [54] J. Song, X.D. Ren, X.S. Li, C.W. Gu, M.M. Zhang, One-dimensional model analysis and performance assessment of Tesla turbine, *Appl. Therm. Eng.* 134 (2018) 546–554.
- [55] G. Manfrida, L. Pacini, L. Talluri, A revised Tesla turbine concept for ORC applications, *Energy Procedia* 129 (2017) 1055–1062.
- [56] G. Manfrida, L. Pacini, L. Talluri, An upgrade Tesla turbine concept for ORC applications, *Energy* 158 (2018) 33–40.
- [57] L. Talluri, D. Fiaschi, G. Neri, L. Ciappi, Design and optimization of a Tesla turbine for ORC applications, *Appl. Energy* 226 (2018) 300–319.
- [58] G. Manfrida, L. Talluri, Fluid dynamics assessment of the Tesla turbine rotor, *Therm. Sci.*, (2019).
- [59] L. Ciappi, D. Fiaschi, P.H. Niknam, L. Talluri, Computational investigation of the flow inside a Tesla turbine rotor, *Energy* 173 (2019) 207–217.
- [60] L. Pacini, L. Ciappi, L. Talluri, D. Fiaschi, G. Manfrida, J. Smolka, Partial admission effects on the flow field of an ORC Tesla turbine, in: *Proceedings of ORC2019, 5th International Seminar on ORC Power Systems*, September 9–11, 2019, Athens, Greece.
- [61] O. Dumont, L. Talluri, D. Fiaschi, G. Manfrida, V. Lemort, Comparison of a scroll, a screw, a piston expander and a Tesla turbine for small-scale organic Rankine cycle, in: *Proceedings of ORC2019, 5th International Seminar on ORC Power Systems*, September 9–11, 2019, Athens, Greece.
- [62] Honeywell, Storage, Handling and Use Guidelines for Solstice®zd Refrigerant, available at: <https://www.honeywell-refrigerants.com/europe/wp-content/uploads/2015/08/Solstice-zd-Handling-Guidelines.pdf>, last accessed on January 2020.
- [63] L. Talluri, O. Dumont, G. Manfrida, V. Lemort, D. Fiaschi, Geometry and performance assessment of Tesla turbines for ORC, in: *Proceedings of ORC2019, 5th International Seminar on ORC Power Systems*, September 9–11, 2019, Athens, Greece.
- [64] SKF, The SKF model for calculating the frictional moment, available at: [https://www.skf.com/binaries/12-299767/0901d1968065e9e7-The-SKF-model-for-calculating-the-frictional-movement\\_tcm\\_12-299767.pdf](https://www.skf.com/binaries/12-299767/0901d1968065e9e7-The-SKF-model-for-calculating-the-frictional-movement_tcm_12-299767.pdf), last accessed on September 2019.
- [65] W.E. Campbell, Studies in Boundary Lubrication, *Trans. ASME* 61 (7) (1939) 633–641.
- [66] S.A. Klein, G.F. Nellis, *Mastering EES, f-Chart software*, 2012.
- [67] W. Traupel, *Thermische Turbomaschinen Zweiter Band Geländerte Betriebsbedingungen, Regelung, Mechanische Probleme, Temperaturprobleme*, Springer-Verlag, New York, (1977).